2. EXPERIMENT 835 AT FERMILAB. THE PHYSICS PROGRAM, THE EXPERIMENTAL APPARATUS AND THE DATA COLLECTION SYSTEM

Experiment E-835 is dedicated to the study of charmonium by resonant formation in $\bar{p}p$ annihilations. It has been carried out at the Antiproton Accumulator of Fermi National Accelerator Laboratory. The data-taking run lasted from October 1996 through September 1997, collecting an integrated luminosity of 143 pb^{-1}. In addition to the charmonium physics results, new high-precision measurements of the timelike form factor of the proton at large momentum transfer are extracted from the data.

The apparatus has been designed to detect electromagnetic final states, which are produced by the antiproton beam in the Accumulator intersecting an internal hydrogen gas jet target. It is a non-magnetic spectrometer, whose main components are a lead-glass electromagnetic calorimeter, a threshold Čerenkov counter, and a tracking system.

Several aspects of the experiment are described in detail in this chapter, emphasizing the information relevant to the form factor analysis.

2.1 Physics Program and Experimental Technique

Experiment E-835 is a collaboration of American and Italian institutions[a]; it studies the spectroscopy of charmonium ($\bar{c}c$), the bound state of a quark c and its antiquark (Figure 2.1).

A large amount of experimental data on charmonium spectroscopy has been obtained at electron-positron colliders. Through the annihilation into a virtual photon, only the states $\psi(nS)$ (like the J/ψ or the ψ'), which have the same quantum numbers of the photon ($J^{PC} = 1^{--}$), can be directly formed. The masses and width of these states have been measured with great precision ($\approx$ hundreds of keV for the masses, $\approx$ tens of keV for the widths), since the initial state was very well known. On the other hand, the other charmonium states are studied by observing the spectrum of the emitted photons in the radiative decays of the ψ', like $\psi' \to \chi_c + \gamma$. In these cases, the measurement of masses and widths is limited by the resolution of the photon detector (a few MeV), and is therefore less precise.

In contrast, the formation of all $\bar{c}c$ states is possible in $\bar{p}p$ collisions, through the coherent annihilation of the quarks in the proton with the antiquarks in the antiproton (Cester and Rapidis 1994). The advantage of this technique is that the precision on the measurement of masses and widths only depends on the knowledge of the beam energy and of its momentum spread. The main limitation is that charmonium signals (typically, 10^2 nb) are immersed in the comparatively huge $\bar{p}p$ total cross section ($\simeq 70$ mb at the J/ψ energy). Therefore, to date, electromagnetic final states have been the only viable method for observing the charmonium resonances.

[a] The complete list of collaborators and other information can be found at `http://www-e835.fnal.gov`.

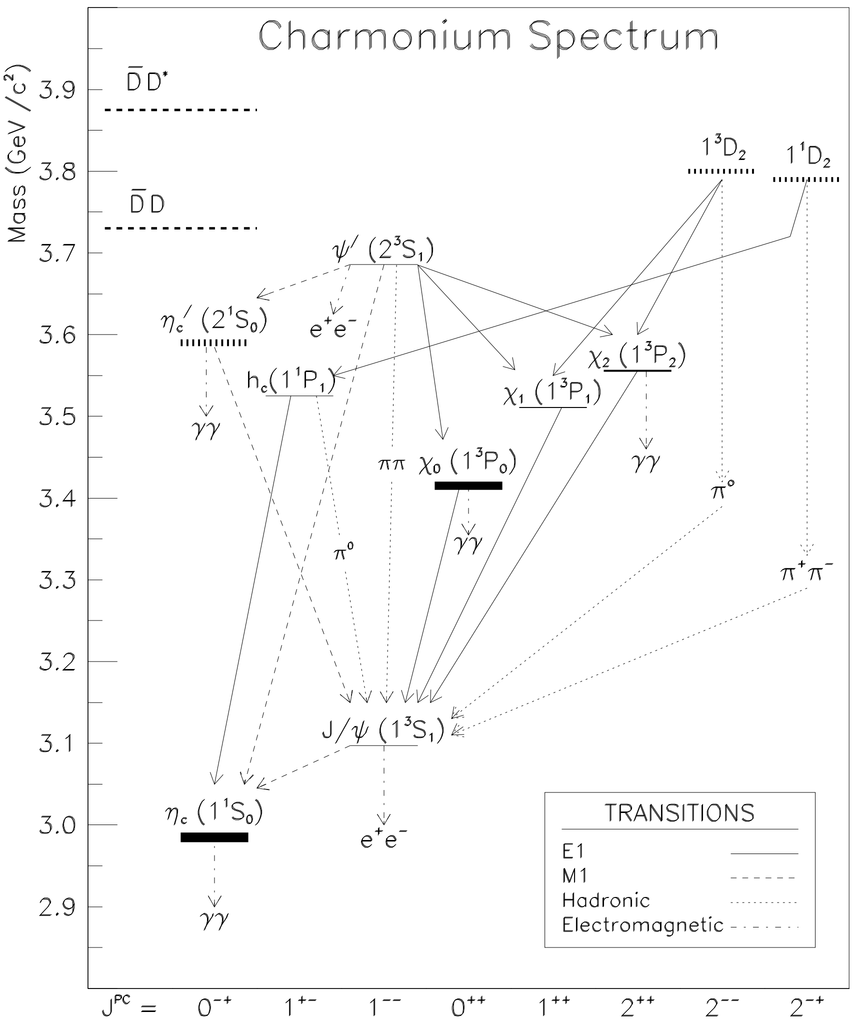

Fig. 2.1: The spectrum of the charmonium system.

The resonances are scanned by varying the beam energy in small steps and by counting, at each energy point, the number of selected events, typically J/ψ-inclusive (with the J/ψ decaying into e^+e^-) or $\gamma\gamma$.

This technique was proposed by Dalpiaz (1979) and used for the first time in 1984 at the CERN Intersecting Storage Ring by experiment R-704. The promising results prompted the design of experiment E-760 at the Fermilab Accumulator, which could exploit better performing beam, target and detector during its data-taking run in 1990–1991. The E-835 detector is an upgrade of the E-760 one. The new components were designed to cope with the increased instantaneous luminosity.

The success of this experimental technique relies on several factors: good knowledge of the beam energy and of its momentum spread, high luminosity, electron/positron identification and hadron rejection at the trigger level, efficient off-line electron reconstruction and precise calorimetry.

Some of these aspects are fundamental for the study of timelike form factors, especially the high luminosity and the low-background electron identification. This series of experiments, E-835 in particular, turned out to provide unique opportunities for studying the magnetic form factor of the proton in the charmonium region ($8 \lesssim s \lesssim 19$ GeV^2), which is the highest q^2 region explored to date, as shown in Section 1.5. Within that region, the choice of luminosity spent at each energy point has been determined by the charmonium physics goals. The results of R-704 and E-760 have been reported by Baglin et al. (1985) and Armstrong et al. (1993), respectively. In this dissertation, I present the results extracted from the E-835 data.

2.2 The Interaction Region: Beam, Target and Luminosity

(a) The Machine

The Fermilab Antiproton Accumulator is a unique machine. Besides its main role as storage ring for $\bar{p}$s to be employed in the Tevatron collider program, it can provide, at lower energies, a high-quality beam of antiprotons, which is desirable for both charmonium and form factor physics. After the shut-down of the CERN Antiproton Accumulator, the Fermilab machine is presently the only one in the world that can play this role[b].

(b) Antiproton Production

A single batch of protons with an intensity of about 3×10^{12} particles is accelerated to 120 GeV in the Main Ring. The eighty-two bunches contained within the batch are extracted from the Main Ring by means of a kicker and transported to the target vault through the AP-1 line (Figure 2.2).

The incident beam is focused to a small spot size using conventional quadrupole magnets and impinges upon the production target, which consists of a stack of nickel disks. The mechanical characteristics of the target (thickness, shape, material, capability of being displaced and rotated) are aimed at limiting the phase space spread of the secondary particles, without compromising the structural integrity of the target itself.

The resulting cone of secondaries is focused by means of a lithium lens, which is a cylinder through which an intense current is forced (Figure 2.3). Lithium is chosen to minimize the absorption of particles passing through

[b] The importance and the operation principles of both antiproton accumulators has been recently discussed by Church and Marriner (1993).

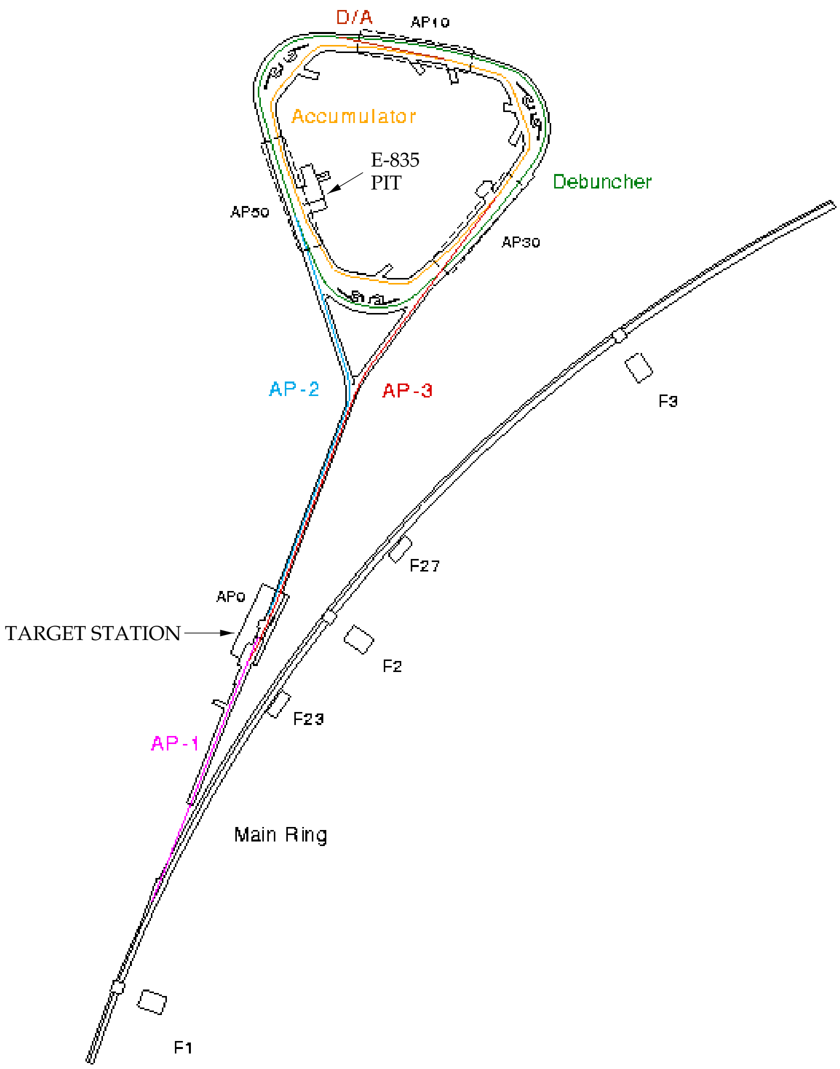

Fig. 2.2: Layout of the Antiproton Source.

the lens. The main advantage of using this kind of lens (compared to quadrupole magnets, for instance) is that one achieves focusing in both the horizontal and vertical planes in a very short distance. At this stage, the time structure of the beam coming off the lens is the same as that of the primary proton beam.

A pulsed dipole magnet bends all particles with the magnetic rigidity p/e of an 8.9 GeV/c antiproton into the AP-2 line, while all other particles are absorbed within a beam dump. The energies of the incident protons and of the collected secondaries are chosen in order to maximize the inclusive antiproton yield, compatibly with the machine constraints.

Particles that survive the trip down the AP-2 line are injected into the Debuncher where they coast for about two seconds. Most of the secondaries decay either in the AP-2 line or in the Debuncher, while electrons are lost due to bremsstrahlung; what is left is solely antiprotons.

On average, about 10^5 protons are needed to obtain a single antiproton. The main causes of inefficiency are the production cross section and the phase-space spread of the outcoming antiprotons. The angular spread de-

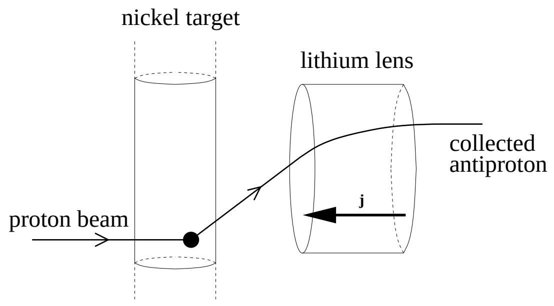

Fig. 2.3: Schematics of the target disks and of the collection lens used for antiproton production. The horizontal and vertical axes are not drawn to scale. The lens is 15 cm long and its diameter is 2 cm.

pends intrinsically on the production mechanism, while the position spread can be controlled by focusing the impinging beam to the smallest possible spot. The momentum aperture of the collection system ($\Delta p/p = 4\%$) also constrains the production efficiency.

In the Debuncher, the momentum spread $\Delta p/p$ of the beam is reduced from 4% to 0.2% through bunch rotation and adiabatic debunching. Betatron (transverse) stochastic cooling is then applied so as to reduce the transverse size of the $\bar{p}$ beam. Momentum (longitudinal) cooling is also applied to further reduce the momentum spread to about 0.1%. Pre-cooling in the Debuncher is done for two reasons: to provide for more efficient momentum cooling in the Accumulator and because of the limited momentum aperture of the Accumulator at injection.

Just before the next pulse arrives from the target, the antiprotons are extracted from the Debuncher and injected into the Accumulator via the D-to-A line. Successive pulses of antiprotons are stacked into the Accumulator core by means of RF deceleration and momentum stochastic cooling. The RF moves (decelerates) the freshly injected pulses of antiprotons from the injection orbit inwards to the edge of the stack tail, the low density portion of the stacked beam. The stack-tail momentum cooling system sweeps the beam deposited by the RF away from the edge of the tail and moves it toward the dense portion of the stack, known as the core, which is close to the inside edge of the Accumulator. Antiprotons are confined in the core by additional longitudinal and transverse cooling.

Antiprotons are stacked for several hours at an average stacking rate of about 3×10^{10} $\bar{p}$/hour, until the desired number, typically 5×10^{11} $\bar{p}$, is achieved.

Over a stacking cycle, this procedure allows to increase the phase-space density of the antiproton beam by a factor of 10^5, somehow compensating for the poor production rate of antiprotons. Instantaneous luminosities comparable with those achievable with proton beams are accessible, both in collider and in fixed-target experiments.

(c) Beam Energy

For the E-835 data taking, the Accumulator operates in an unconventional manner. After stacking at 8.9 GeV, the beam needs to be decelerated so that collisions with the protons in the target take place at the desired CM energy, corresponding to the particular charmonium resonance under study (Table 2.1). Often, for instance in the case of the η_c and of the J/ψ, the transition energy of the machine ($\gamma_t = 5.430$, corresponding to $\sqrt{s} = 3.365$ GeV) has to be crossed.

The deceleration is carried out at a rate of about 20 MeV/s and consists of several steps or ramp points. The deceleration ramp is an empirical table

Charmonium Resonance	Formation Energy (GeV)	Beam Momentum (GeV/c)
$\eta_c(1^1S_0)$	2.980	3.676
$J/\psi(1^3S_1)$	3.097	4.066
$\chi_{c0}(1^3P_0)$	3.417	5.201
$\chi_{c1}(1^3P_1)$	3.511	5.550
$\chi_{c2}(1^3P_2)$	3.556	5.725
$\psi'(2^3S_1)$	3.686	6.232

Tab. 2.1: Antiproton beam momentum corresponding to the formation energy of some charmonium resonances. Their masses are taken from Caso et al. 1998.

of magnet currents for each beam energy. After each step, the accelerator parameters, such as the orbit, the tunes, the dispersion and the chromaticity, are measured and possibly corrected. Once the desired energy is reached, the jet target is turned on and the data taking begins.

The CM energy $\sqrt{s}$ is calculated from the beam energy[c] E_{beam}, which in its turn is obtained by measuring the revolution frequency f and the orbit length L of the beam; the product $f \cdot L$ is the speed β of the antiprotons:

$$\begin{aligned} \sqrt{s} &= \sqrt{2} m_p (1+\gamma)^{1/2} \\ \gamma &= E_{beam}/m_p = \left(1-\beta^2\right)^{-1/2} \\ \beta &= fL. \end{aligned} \tag{2.1}$$

The relative error on the CM energy is the sum in quadrature of the relative errors on the revolution frequency and on the orbit length, multiplied by an energy-dependent factor:

$$\frac{\delta\sqrt{s}}{\sqrt{s}} = \left[\frac{\beta^2\gamma^3}{2(1+\gamma)}\right] \cdot \sqrt{\left(\frac{\delta f}{f}\right)^2 + \left(\frac{\delta L}{L}\right)^2}. \tag{2.2}$$

In the charmonium region, this factor varies between 5 and 45, as shown in Figure 2.4. The length of the Accumulator is 474 m, making the revolution frequency approximately 0.6 MHz. This means that, in order to get a CM energy error of $\approx 10^2$ keV one has to know f to about one Hertz and L to about one millimeter[d].

The Schottky noise of the beam is suitable for such high-precision measurements of the revolution frequency. It is also used to monitor the momentum spread of the beam, through the relation

$$\frac{\Delta p}{p} = \frac{1}{\eta}\frac{\Delta f}{f}, \tag{2.3}$$

[c] The speed of the molecules of the jet target (~ 800 m/s) can be neglected.

[d] Such small uncertainty is required for some of the charmonium resonances, but it is not necessary for the form factors, for which different energy regions can be combined together.

where η is the slip factor of the machine. The beam energy spread, as measured from the Schottky spectrum, is shown in Figure 2.5 for each data-taking run[e].

The orbit length is calibrated by scanning the ψ' resonance, whose mass is known with an uncertainty of 90 keV and where the factor defined in Equation 2.2 is relatively large. A reference orbit with length $L_0 = 474.050 \pm 0.001$ m is defined, and the values read out by the Beam Position Monitors (BPMs) are recorded. For all other energies, the orbit length $L = L_0 + \Delta L$ is computed by comparing the readings of the BPMs with the reference ones, in order to measure ΔL. This is possible because ΔL is related to the orbit displacements inside the 38 dipole magnets, which in their turn can be computed by knowing the lattice functions and the displacements at the 48 horizontal BPMs, measured with an uncertainty of half a millimeter (Garzoglio

[e] The first bin (null energy spread) contains the seventy-one runs for which the link between the accelerator network and the data-acquisition system failed. The data was not recorded, but the frequency spectrum had been checked on-line.

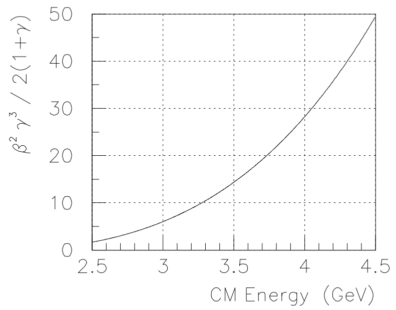

Fig. 2.4: The energy dependence of the error amplification factor defined in Equation 2.2

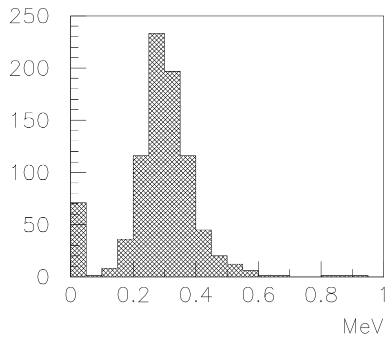

Fig. 2.5: The CM energy spread of the beam for each of the 866 data-taking runs.

1998).

With this procedure, the CM energy can be determined to less than a hundred keV. Due to a malfunction of some of the BPM systems for part of the run, a significant systematic error must be taken into account. For the present analysis, one can rely on the fact that the total error $\delta\sqrt{s}$ never exceeds 2 MeV; its systematic impact on the form factor (measured by the slope $d\,|G_M|\,/d\sqrt{s}$) is still negligible compared to the total measurement error $\delta\,|G_M|$ on the form factor itself:

$$\delta\,|G_M| \gg \left|\frac{d\,|G_M|}{d\sqrt{s}}\right| \cdot \delta\sqrt{s}, \tag{2.4}$$

as can be deduced, for instance, from Figure 3.22.

(d) The Jet Target

Since antiproton beams are a precious resource, it is particularly important to use them efficiently, especially when the process under study has a low

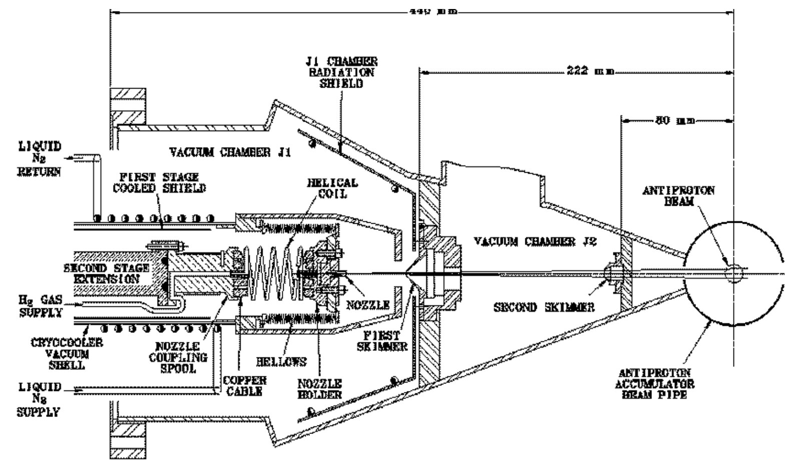

Fig. 2.6: Schematics of the internal hydrogen gas jet target.

cross section and the total integrated luminosity is a relevant factor. An internal hydrogen gas jet target is suitable for this task.

The E-835 target (Allspach et al. 1998) intersects the circulating antiproton beam, as shown in Figure 2.6. The helium refrigerated expansion stage causes the formation, inside the nozzle, of H_2 cluster streams with densities up to $\rho = 3.2 \times 10^{14}$ atoms/cm^3. The core of the cluster stream is selected by aligning the movable nozzle with two skimmers. A series of pumps (not shown in the figure), in conjunction with the alignment system of the jet, maintains a low level of background gas inside the beam pipe. Consequently, the antiproton stochastic cooling is sufficient to contain the beam emittance growth due to the presence of the target itself.

The total transverse width of the jet at the interaction point is less than 7 mm, as inferred from measurements of the density profile (Figure 2.7a).

In Figure 2.7b, the set of operating conditions is shown. For each value P of the pressure[f], the corresponding temperature T (open circles, right vertical axis) and density ρ (full circles, left axis) are plotted. The closer the P-T points (open circles) are to the saturation curve, the higher the achieved density is. A trade-off is found between high density and the possible formation of liquid, which could freeze and obstruct the nozzle.

During a data-taking run, as the beam current decreases, the target density is varied so as to keep the instantaneous luminosity constant, around 2×10^{31} cm^{-2} s^{-1}. This value is close to the maximum rate that the data-acquisition system can keep up with; therefore the integrated luminosity collected by the experiment is maximized.

[f] 1 psi = 6.9×10^3 Pa; 14.7 psi = 1 atm

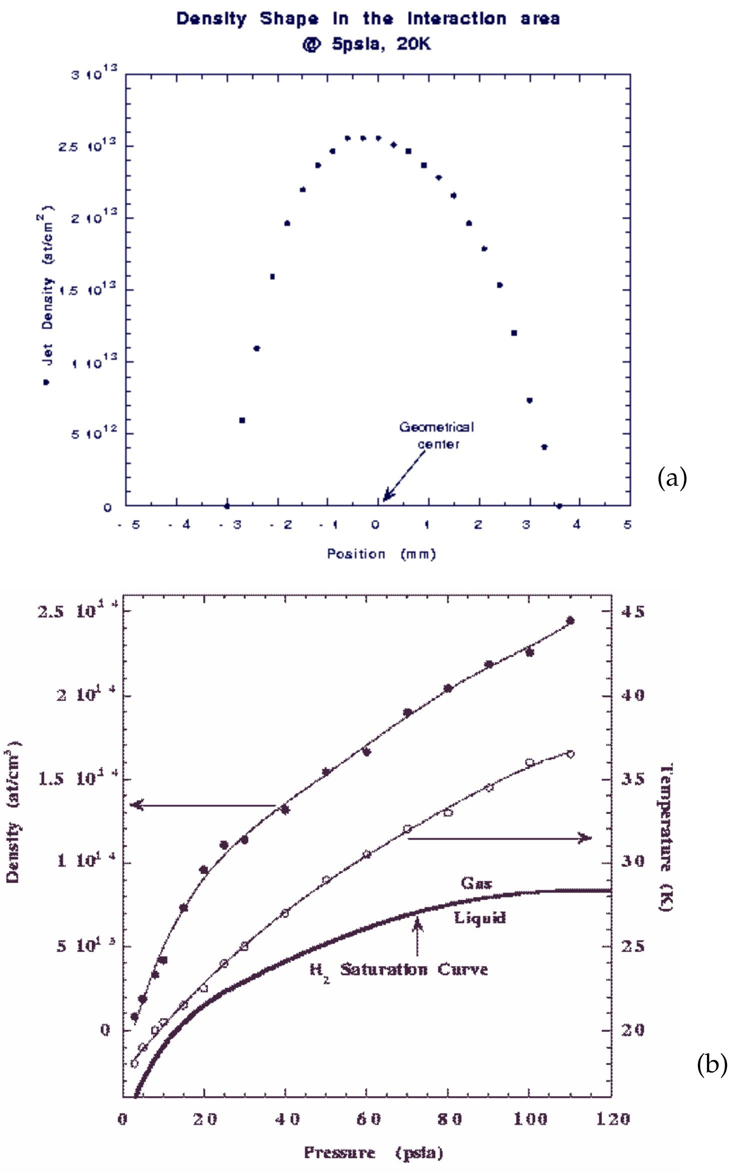

Fig. 2.7: Jet target performance: (a) Density profile of the cluster stream. (b) Target density as a function of pressure and temperature.

(e) Accumulated Luminosity

Luminosity measurement. The luminosity is measured by observing the recoil protons corresponding to forward angle elastic scattering of antiprotons.

The number N of protons scattered within the solid angle Ω in a given time interval is proportional to the integrated luminosity L:

$$N = L \int_{\Omega} \left(\frac{d\sigma}{d\Omega} \right) d\Omega, \tag{2.5}$$

where $d\sigma/d\Omega$ is the $\bar{p}p$ elastic differential cross section, which has been measured with good accuracy in the energy range of interest for E-835 (Armstrong et al. 1996).

The luminosity monitor (Trokenheim et al. 1994; Pedlar 1998) is located about 150 cm below the interaction point, at a polar angle of 86.4° (Figure 2.8 and Figure 2.11). It consists of three solid state detectors, enclosed in a vacuum vessel directly coupled to the beam pipe. The presence of three devices allows to detect possible horizontal displacements of the beam; it also provides redundancy in case of failure of one of them. One of the de-

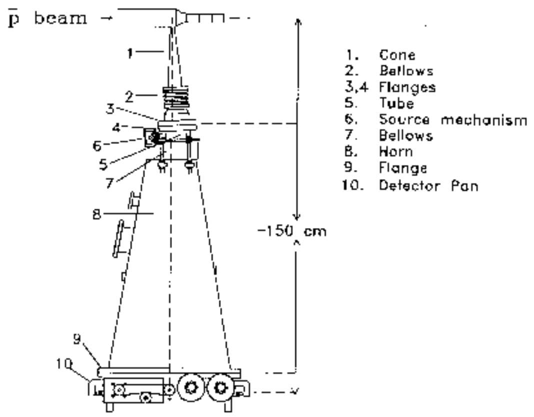

Fig. 2.8: Layout of the luminosity monitor.

tectors sits on a movable tray and is situated directly beneath the beam axis. The other two are fixed and lie on either side. The active surface of the three detectors is 1×5 cm^2; their thickness is 0.5 mm.

In the angular region covered by the detectors, the scattered protons possess a kinetic energy that varies between 3 MeV and 7 MeV (depending strongly upon the beam momentum and upon the scattering angle), which correspond to a penetration range smaller than 0.4 mm.

The analog signal from each detector is sent to an ADC and then to a histogramming memory, which acts as a multichannel spectrum analyzer. Each of its four channels has 8192 24-bit bins. Every two minutes, and at the start and finish of each data-taking run, the contents of the histogramming memory are recorded and then reset to zero.

About 10^5 events are present in the elastic recoil peak for 10^2 nb^{-1} of integrated luminosity. Figure 2.9 shows a typical energy spectrum. Each bin is 17.4 keV wide. Data were taken at the energy of the χ_{c2} resonance (run number 695, $\sqrt{s} = 3556.56$ MeV, instantaneous luminosity $\mathcal{L} = 1.7 \times 10^{31}$ cm^{-2} s^{-1}), corresponding to a total of 36.8 nb^{-1}.

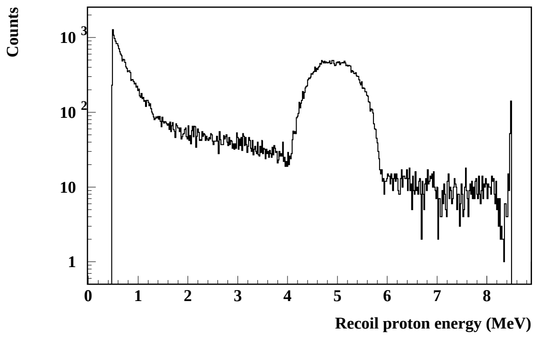

Fig. 2.9: Energy spectrum of recoil protons detected by the luminosity monitor (description in the text).

The uncertainty on each luminosity measurement is less that 3%; the main source of error (2%) is the value of the differential cross section.

Running conditions. Typically, data are taken at an instantaneous luminosity $\mathcal{L}$ of 1.9×10^{31} cm^{-2} s^{-1} (above the transition energy of the machine, $\sqrt{s} = 3.365$ GeV) or 0.9×10^{31} cm^{-2} s^{-1} (below transition). The difference is mostly due to the fact that transition crossing is more efficient with smaller-sized beams; therefore, it was chosen to use antiproton stacks of modest intensity (~ 20 mA, corresponding to 2×10^{11} particles) for low-energy data-taking. Figure 2.10a shows the instantaneous luminosity versus the CM energy for all runs; the areas of the boxes are proportional to the amount of data (ie total luminosity) collected at each value of $\sqrt{s}$ and $\mathcal{L}$.

During the whole E-835 run, which lasted for about one year, the experiment has accumulated 143 pb^{-1}. In Figure 2.10b, the integrated luminosity as a function of time is reported.

2.3 The Detector

The E-835 apparatus has been designed to detect electromagnetic final states. It makes use of some of the components employed in experiment E-760 (Armstrong et al. 1993) as well as several upgrades. The layout of the detector is shown in Figure 2.11. It is a non-magnetic spectrometer with full azimuthal (ϕ) coverage and polar angle (θ) acceptance ranging from 2° to 70°. The central detector ($15° < \theta < 65°$) has cylindrical symmetry around the beam axis; its main components are the lead-glass electromagnetic calorimeter (CCAL), the threshold gas Čerenkov counter and the inner tracking system.

Upstream ($\theta = 65°$), the polar coverage is limited by constraints of space

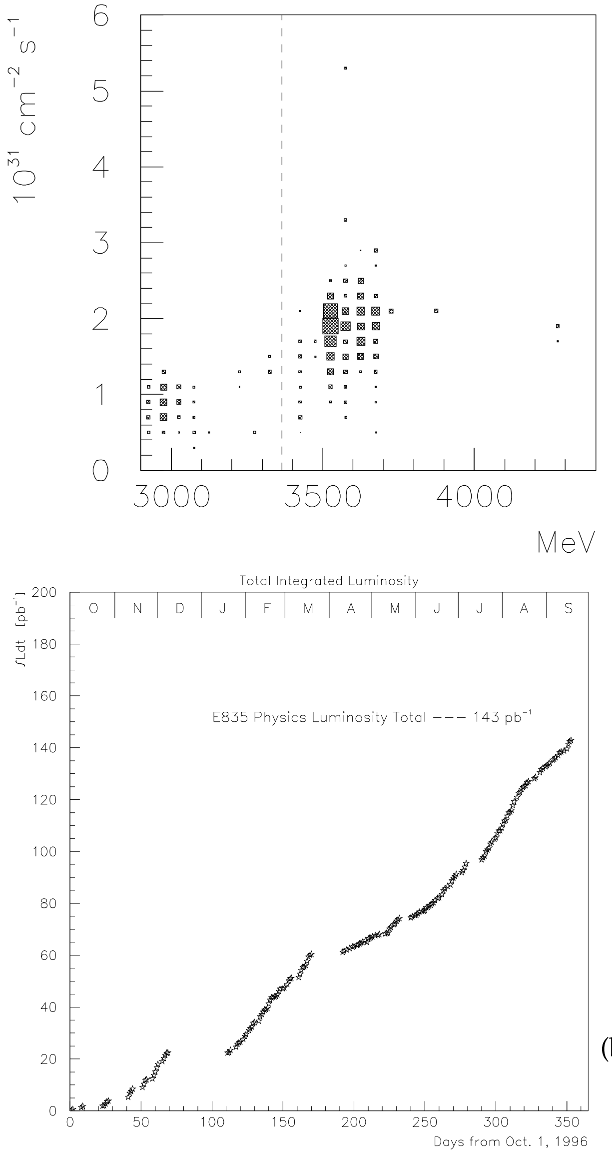

(a)

(b)

Fig. 2.10: E-835 luminosity. (a) The instantaneous luminosity versus the CM energy. The vertical dashed line represents the transition energy of the antiproton accumulator. (b) The integrated luminosity accumulated throughout the data-taking run.

(jet target and luminosity monitor equipment). Given these constraints, the choice of the downstream edge of the detector ($\theta = 15^{\circ}$) represents a compromise between several factors: the geometrical acceptance for the reactions of interest, mostly $\bar{p}p \to \gamma\gamma$, $\bar{p}p \to e^{+}e^{-}$ and $\bar{p}p \to J/\psi + X \to e^{+}e^{-} + X$; the interaction and trigger rates; the radiation damage, especially in the lead glass; the speed of the hadrons in the final state, which affects the rejection power of the Čerenkov counter.

(a) Electromagnetic Calorimeter

The central calorimeter (CCAL) (Bartoszek et al. 1991) measures the energy and direction of photons, electrons and positrons.

One of the most important CCAL design goals is an effective background rejection. The neutral electromagnetic final states of charmonium formed in $\bar{p}p$ annihilations are immersed in a hadronic background, which consists mostly of neutral pions decaying into two photons. Identifying

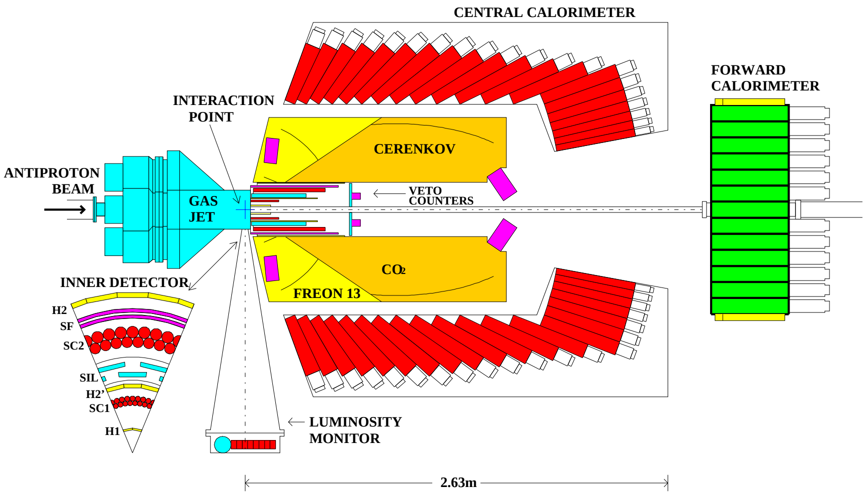

Fig. 2.11: The E-835 Detector.

Block Number	Block Length (cm)	Central θ (deg)	Block Width (deg)	Distance from Target (cm)	PMT Diameter (inches)	Fractional PMT Coverage
01	37.80	67.387	5.226	72.44	3.0	0.473
02	38.65	62.259	5.031	75.87	3.0	0.475
03	39.88	57.342	4.803	80.07	3.0	0.476
04	41.50	52.664	4.552	85.08	3.0	0.478
05	43.54	48.246	4.284	90.96	3.0	0.479
06	46.03	44.101	4.007	97.79	3.0	0.481
07	48.98	40.234	3.728	105.62	3.0	0.482
08	50.00	36.644	3.451	114.54	3.0	0.497
09	50.00	33.327	3.183	124.66	3.0	0.520
10	50.00	30.273	2.925	136.07	3.0	0.544
11	50.00	27.472	2.679	148.89	3.0	0.568
12	50.00	24.908	2.449	163.26	3.0	0.593
13	50.00	22.567	2.233	179.34	3.0	0.617
14	50.00	20.434	2.033	197.28	3.0	0.641
15	50.00	18.493	1.848	197.29	2.5	0.546
16	50.00	16.730	1.678	197.29	2.5	0.664
17	50.00	15.130	1.522	197.30	2.0	0.527
18	50.00	13.679	1.380	197.30	2.0	0.644
19	50.00	12.364	1.250	197.30	1.5	0.443
20	50.00	11.174	1.131	197.30	1.5	0.543

Tab. 2.2: Dimensions, positions and photomultiplier characteristics of the 20 lead-glass blocks within each of the 64 CCAL wedges.

and rejecting these events requires: (a) good position resolution, which implies fine segmentation; (b) sensitivity to low-energy showers, which limits the thickness of the detector. In fact, high position resolution is necessary for symmetric pion decays, ie when the two emerging photons have approximately the same energy; on the other hand, a low energy threshold is important when the decay is asymmetric.

The calorimeter is a matrix of 1280 lead glass Čerenkov counters (64 *wedges* in ϕ by 20 *rings* in θ, shown in Figure 2.12), read out with photomultiplier tubes (PMTs). Each block is pointing towards the interaction region. The thickness of the blocks, expressed in radiation lengths ($X_0 = 3.141$ cm), varies between $12X_0$ and $16X_0$. In Table 2.2 some of the mechanical characteristics of the CCAL are reported.

The angular resolution is 11 mrad in ϕ and 6 mrad in θ; it includes the uncertainty on the location of the interaction vertex. The average energy resolution is $\sigma_E/E = 1.4\% + 6\%/\sqrt{E(\mathrm{GeV})}$.

The signal from each block is sent to a shaper board and then to an ADC. Each CCAL channel is also equipped with a time-to-digital converter (TDCs), which provides the timing information needed to reject pile-up clusters. For showers with energy above 80 MeV, the time is always recorded; they are classified as 'in time' or 'out of time'. Clusters with smaller energies are identified as 'undetermined' if such information is missing.

(b) Čerenkov Counter

The threshold gas Čerenkov counter (Biino et al. 1992; Bagnasco et al. 1998b) is used for identifying electrons and positrons. It has been designed to reject pions and heavier particles both at the trigger level and off-line.

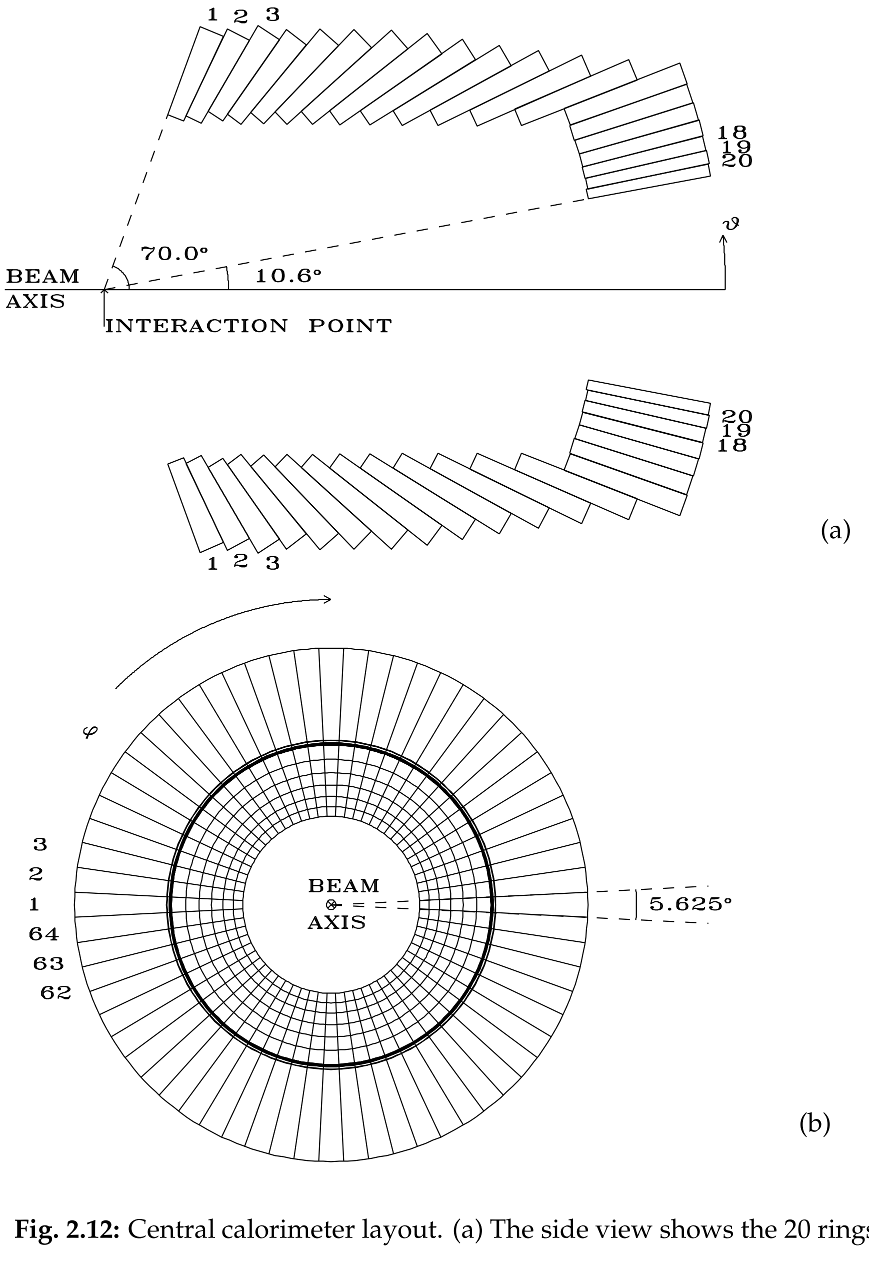

Fig. 2.12: Central calorimeter layout. (a) The side view shows the 20 rings. (b) Cross section showing the 64 wedges.

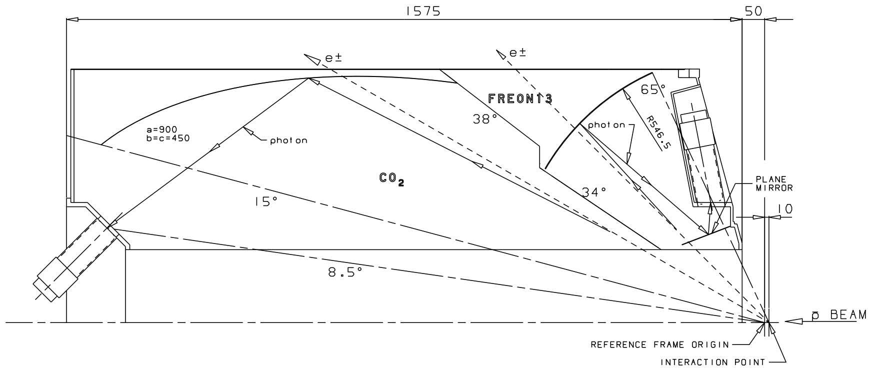

Fig. 2.13: Schematic side view of the Čerenkov counter. One of the downstream cells (CO_2 gas, elliptical mirror) and one of the upstream cells (Freon-13 gas, spherical mirror) are visible. Dimensions are in mm.

Characteristics	Downstream Cells	Upstream Cells	
Polar Coverage	15°–38°	34°–65°	
Azimuthal Segmentation	45° × 8	45° × 8	
Radiator Length	93–72 cm	34–39 cm	
Gas at STP	CO_2	Freon-13	Freon-12
Index of Refraction $(n - 1)$	4.1×10^{-4}	7.2×10^{-4}	10.8×10^{-4}
θ_c from $\cos\theta_c = 1/n$	1.64°	2.17°	2.66°
Pion Threshold (GeV/c)	4.873	3.677	3.003
Light Collection Efficiency	0.84–0.90	0.84–0.98	0.75–0.88

Tab. 2.3: Characteristics of the Čerenkov counter.

The counter occupies a cylindrical sector around the beam pipe (inner radius = 17 cm, outer radius = 59 cm). It consists of 16 gas tight cells (two in θ by eight in ϕ), covering the whole azimuth and the polar region between 15° and 65°. Each cell is equipped with a photomultiplier tube and is read out by an ADC and a TDC. Figure 2.13 shows a schematic diagram of a sector the counter. Some of its characteristics are summarized in Table 2.3.

The faster particles that must be rejected are the pions from $\bar{p}p \to \pi^+\pi^-$. The relativistic factor $\gamma_\pi = (1 - \beta_\pi)^{-1/2}$ of these pions as a function of the laboratory angle θ is plotted in Figure 2.14. The curves correspond to the formation energies of the J/ψ ($\sqrt{s} = 3.097$ GeV) and of the ψ' ($\sqrt{s} = 3.686$ GeV). Two different gases at room temperature and atmospheric pressure are used in the cells: (a) CO_2 downstream ($15° < \theta < 38°$), where particles are faster and where the thickness of the radiator is longer; (b) Freon-13 (CF_3Cl) upstream ($34° < \theta < 65°$), so that the shorter radiator length is compensated by a higher index of refraction[g].

The limited size of the interaction region and the small value of the Čerenkov angle θ_c, make it possible to use a relatively straightforward light collection system. In the upstream cells, a spherical and a plane mirror direct the light towards the photomultiplier tube, located in a recess on the wall of the cell. In each of the downstream cells is an ellipsoidal mirror; one of its foci lies in the interaction region, while the other one coincides with the face of the PMT. The light collection efficiency reported in Table 2.3 includes the geometrical acceptance (calculated), the transmittance of the radiator (calculated) and the reflectance of the mirrors (measured).

The detection efficiency of the counter has been measured with a sample of clean events $\bar{p}p \to e^+e^-$ and $\bar{p}p \to \chi_{c2} \to J/\psi + \gamma \to e^+e^- + \gamma$,

[g] During the last month of data taking, Freon-12 (CF_2Cl_2) was used instead of Freon-13. The performance of the detector did not change significantly.

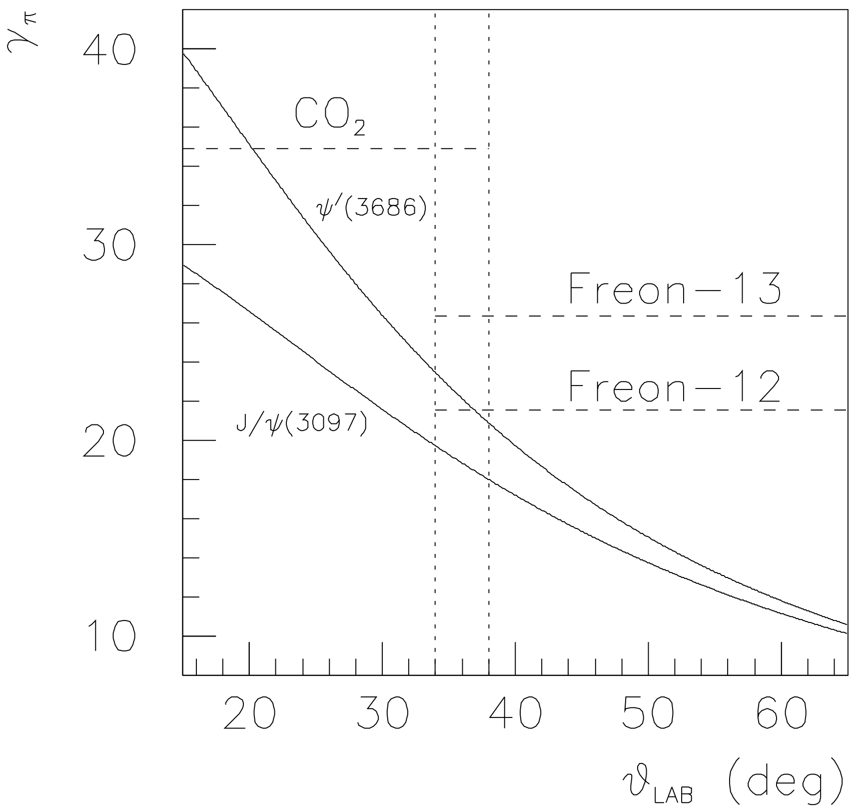

Fig. 2.14: The relativistic factor γ_π as a function of the polar angle θ for pions from $\bar{p}p \to \pi^+\pi^-$ at two different CM energies. The vertical dotted lines represent the edges of the cells. The three horizontal dashed segments indicate the pion thresholds for each gas.

Characteristics	Scintillating Fibers	Clear Fibers
Type	Kuraray	Kuraray
	SCSF-3HF-1500 Multiclad	Multiclad
Diameter (μm)	835	835
Core Diameter (μm)	740	740
Length (m)	$\simeq$ 0.95	$\simeq$ 2.2
Attenuation Length (m)	5.5±0.3	10.4±0.5

Tab. 2.4: Fiber characteristics.

selected with no requirements on the Čerenkov counter itself. It comes out to be $(98.1 \pm 0.5)\%$.

Besides the overall light collection efficiency, the average number of photoelectrons $\langle n_{phe} \rangle$ collected per electron or positron depends upon the thickness of the radiator, the speed of the particle and the quantum efficiency of the PMTs. The one-photoelectron equivalent in ADC counts has been measured periodically by recording the thermal noise spectrum of the PMTs. The average number of photoelectrons is $\langle n_{phe} \rangle = 14$–$16$ for the downstream cells and $\langle n_{phe} \rangle = 8$–$9$ for the upstream cells.

(c) Scintillating Fiber Tracker

The main purpose of this 860-channel cylindrical tracker (Ambrogiani et al. 1997; Ambrogiani et al. 1998) is to measure the polar angle θ of charged tracks with high precision, in the region $15° < \theta < 65°$. Its prompt signal is also used in the first level trigger, to select hadronic channels (like $\bar{p}p$ elastic or $\bar{p}p \to \phi\phi \to K^+K^-K^+K^-$) based upon their kinematic characteristics. In addition, the good overall light yield makes it possible to combine the pulse height information and the fine granularity to discriminate between

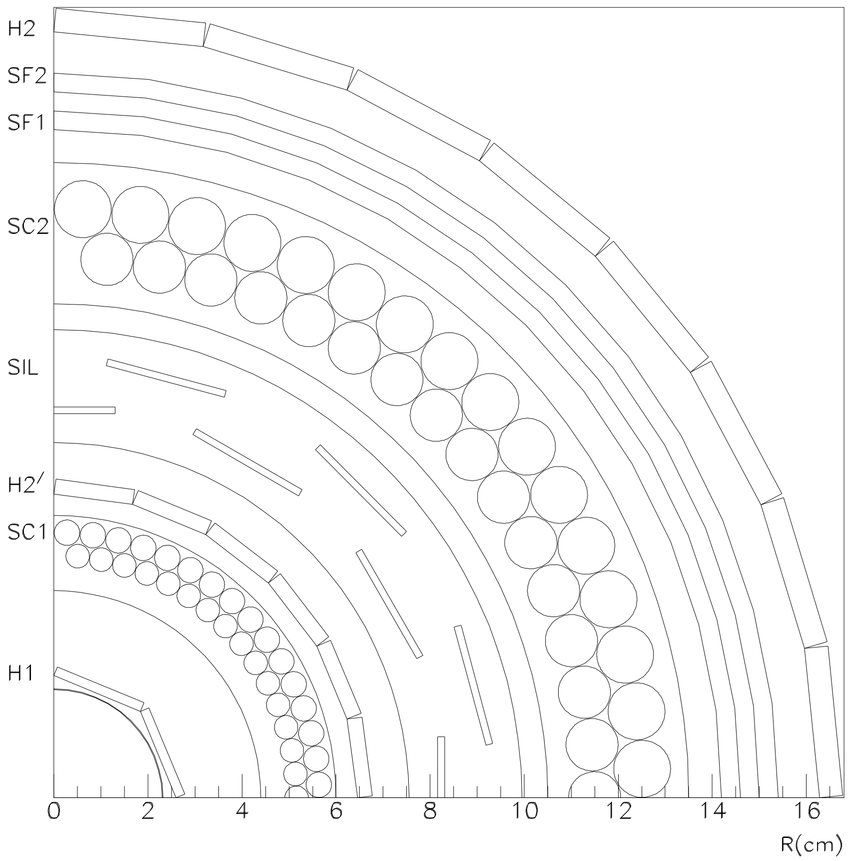

Fig. 2.15: Schematic cross section of the inner detectors: (a) the three hodoscopes (H1, H2′ and H2); (b) the two straw chambers (SC1 and SC2); (c) the two layers of scintillating fibers (SF1 and SF2); (d) the silicon detector (SIL).

Characteristics	Inner Layer	Outer Layer
Average Radius (mm)	144.0	150.6
Pitch (mm)	1.10	1.15
Number of Fibers	430	430

Tab. 2.5: Mechanical characteristics of the scintillating fiber tracker.

single minimum-ionizing particles and e^+e^- coalescent pairs, which constitute one of the main sources of background (Section 3.4). This last feature has not been implemented, since we already have an efficient and powerful off-line tool to tag single electrons or positrons, ie the Electron-Weight index, described in Section 3.1.(c).

Each scintillating fiber is wound around one of the two support cylinders, on the surface of which a set of U-shaped grooves has been machined. The depth of the grooves varies linearly with the azimuthal coordinate ϕ, so that the fiber overlaps itself after one turn (Figure 2.16). Some of the characteristics of the fibers and of the cylinders are summarized in Table 2.4 and in Table 2.5. On one end, the fibers are aluminized, to increase the light yield and to improve its homogeneity; on the other end, they are thermally spliced to clear fibers, which, after a four-meter path, bring the light to the surface of the Visible Light Photon Counters (VLPC HISTE-V, EOC-low). The complete light path is shown in Figure 2.17.

The VLPCs (Petroff and Atac 1989; Atac 1998) are solid state photodetectors[h] with high quantum efficiency (70% at 550 nm), gain of about 2×10^4, single-photon counting capability and resistance to rates up to 10^8 photons/pixel/s. They are housed in a cryostat and operated at a temperature

[h] In the review article by Ruchti (1996), a discussion of the paradigm for scintillating fiber trackers read out with visible-light photon counters can be found.

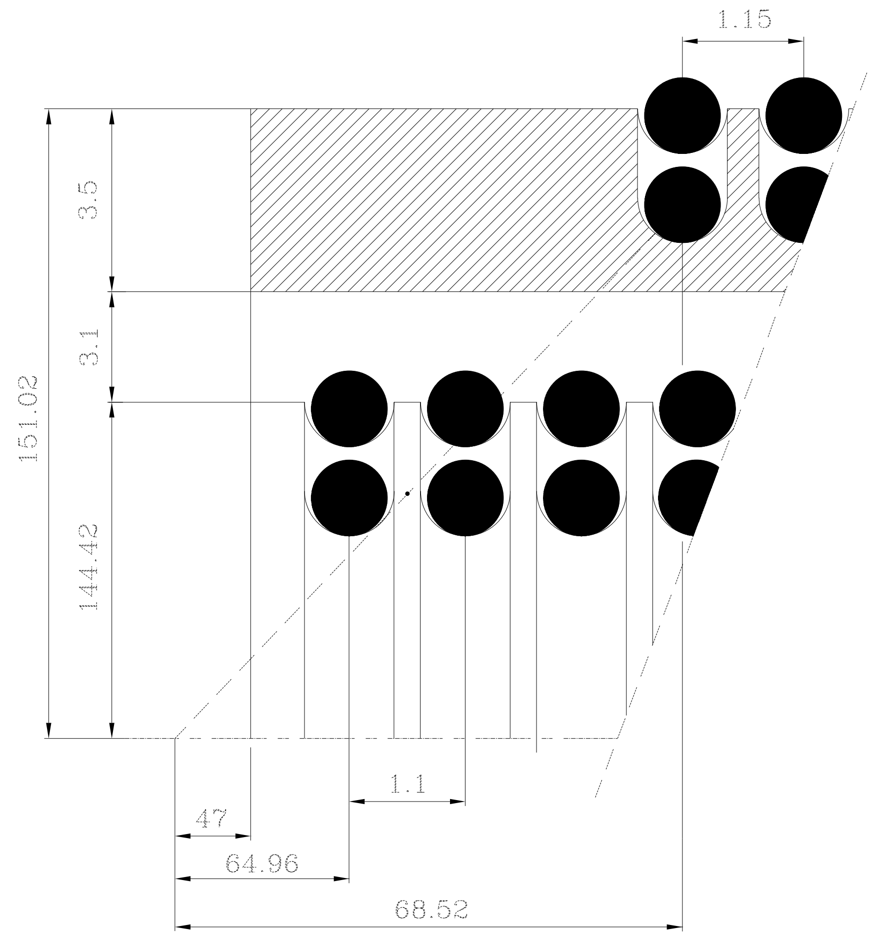

Fig. 2.16: Side view of the two support cylinders of the fiber tracker (dimensions in millimeters, not drawn to scale). Both ends of each scintillating fiber are shown (black circles).

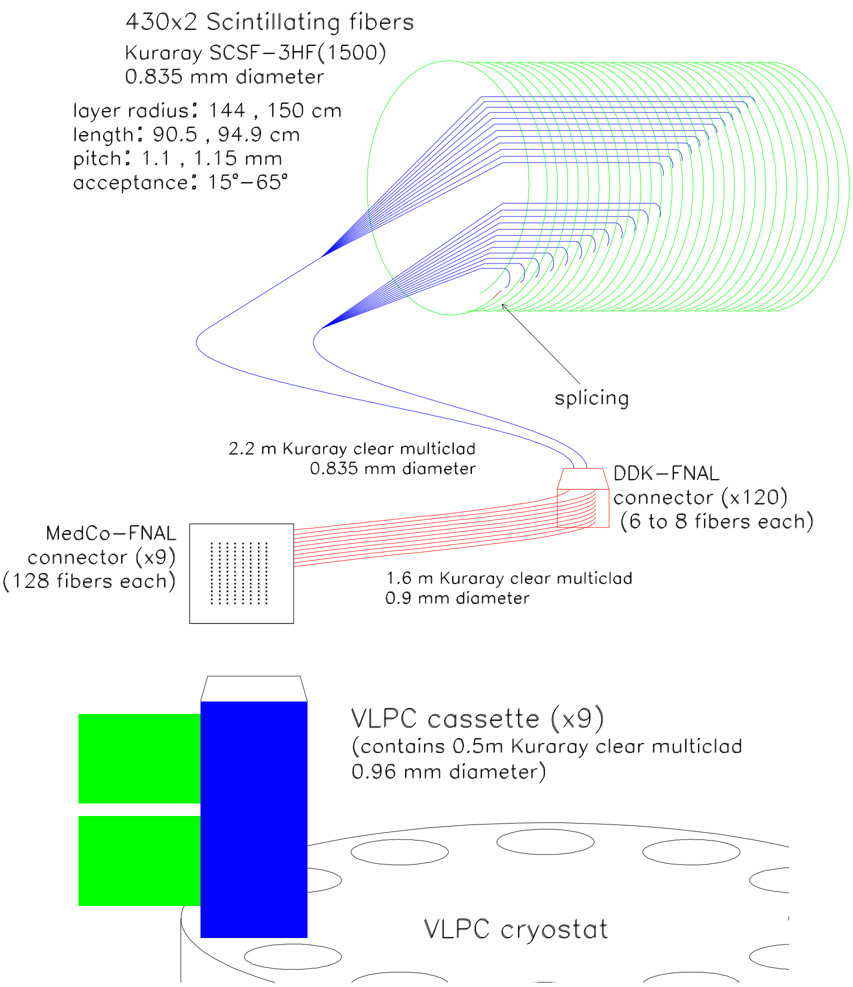

Fig. 2.17: Diagram of the light path from the scintillating fibers to the VLPC cryostat.

of 6.5 K.

The electronic signal generated by the VLPCs is amplified and sent to discriminator-OR-splitter modules. These modules provide an analog and a digital output for each input channel, together with the digital OR of all inputs. The analog signal is recorded by ADCs, while the digital output is read out by latches. The digital OR of a set ('bundle') of adjacent channels is sent to TDCs and to the first-level trigger logic.

For each channel, we measured the one photoelectron equivalent in ADC counts by illuminating the VLPC pixels with an attenuated LED source. From a high statistics sample ($\approx 10^3$ hits/fiber) of hadronic punch-through tracks in the central calorimeter, we obtained the charge generated by a minimum-ionizing particle. The resulting average number of photoelectrons per mip is about 14 — the high quantum efficiency of the VLPCs compensates for the thinness of the active material.

The detection efficiency and the tracking resolution have been measured with a clean sample of J/ψ-inclusive and ψ' events, where the J/ψ or the ψ' decays into e^+e^-.

In Figure 2.18a, I report the fraction of tracks detected by the tracker, as a function of the polar angle θ for different data samples. The variations over time are due to different running conditions (VLPC bias voltage, ADC gate width, dead channels). The decrease in the upstream region ($\theta > 40°$) is consistent with the diminished geometrical acceptance (due to the constant fiber spacing), evaluated with a Monte Carlo calculation; the average detection efficiency is 99.5%.

The fiber tracker is by far the device with the best θ resolution in the E-835 apparatus. For this reason, I measured its 'intrinsic' resolution, defined as the standard deviation (divided by $\sqrt{2}$) of the distribution of the residuals $\theta_{INN} - \theta_{OUT}$, where, for a given track, θ_{INN} (θ_{OUT}) is the polar angle measured with the inner (outer) layer (Figure 2.18b). The intrinsic resolution, averaged over all polar angles, is 0.7 ± 0.1 mrad.

(d) Straw Chambers

Two cylindrical straw chambers (Bagnasco et al. 1998a) provide a measurement of the azimuthal coordinate ϕ for charged tracks.

Each chamber consists of two staggered layers of 64 drift tubes, with their axes parallel to the beam pipe (Figures 2.15 and 2.19). This geometry allows to achieve a relatively low occupancy in each element and to solve the left-right ambiguities on the position of the track with respect to the anode wire. The main characteristics of the two chambers are reported in Table 2.6.

The tubes contain a mixture of Ar, C_4H_{10} and $(OCH_3)_2CH_2$, in the pro-

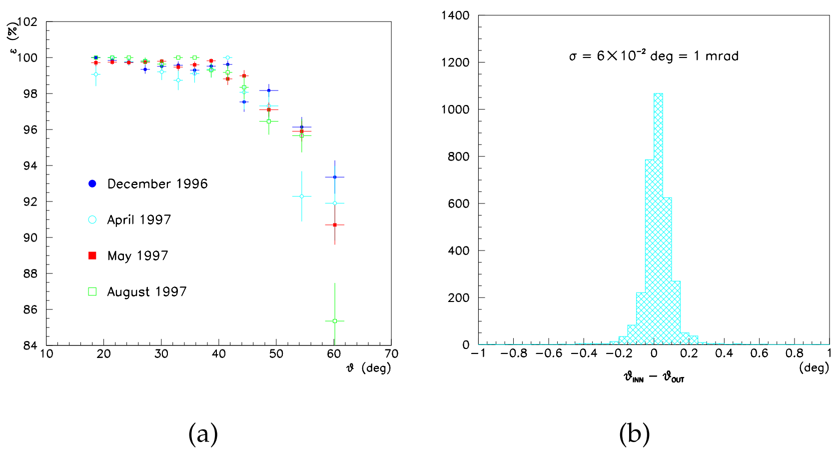

Fig. 2.18: Detector performance of the scintillating fiber tracker: (a) detection efficiency $\times$ geometrical acceptance; (b) distribution of residuals.

Characteristics	Inner Chamber	Outer Chamber
Average Radius (mm)	54	120
Polar Coverage	15°–58°	15°–65°
Diameter of Tubes (mm)	5.0, 5.4	11.1, 12.1
Length of Tubes (mm)	182	414
Operating Voltage (V)	1320	1530
Anode diameter (μm)	20	20

Tab. 2.6: Main characteristics of the straw chambers.

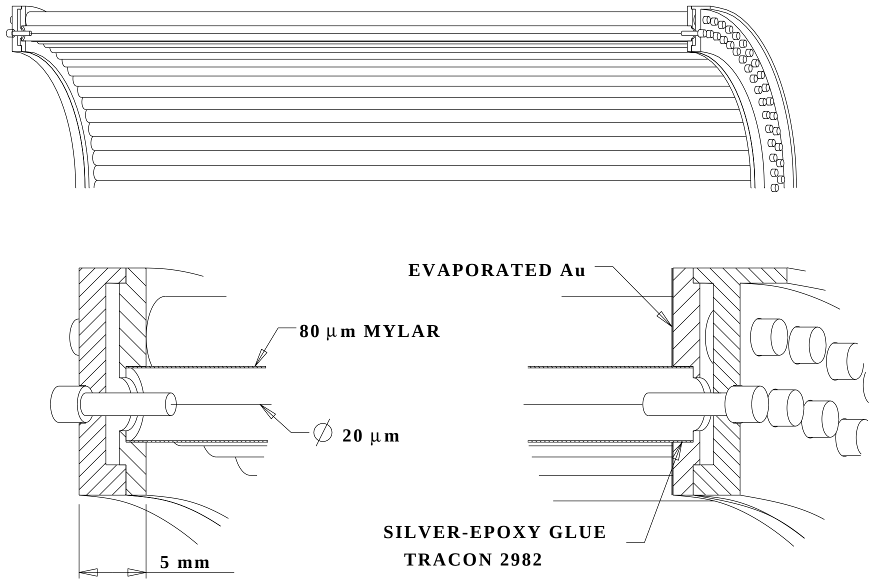

Fig. 2.19: Schematic diagram of the inner straw chamber and a detail of the anode wire holders.

portion 82:15:3 (drift velocity of about 40 μm/ns). This gas is chosen because it shows good detection efficiency at relatively low voltage and because it can cope with the high event rates (~ 10^2 kHz/tube). Each of the 128 channels is read out by an amplifier-shaper-discriminator directly mounted on the downstream end of the detector. The output signals are then sent to a TDC.

The detection efficiency per layer varies between 0.8 (near the walls of the tubes) and 1 (in proximity of the anode wire), as shown in Figure 2.20a. The angular resolution per track is measured with a clean sample of events $\bar{p}p \to J/\psi \to e^+e^-$. It is 9 mrad per track, corresponding to about 250 μm per layer (Figure 2.20b).

(e) Silicon Pads

A silicon pad detector (Buzzo et al. 1997) to be used for tracking was built and installed, but never exploited because of the excessive electronic noise.

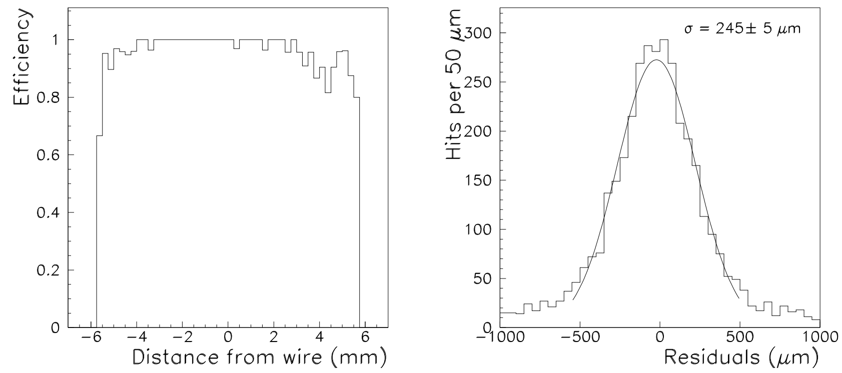

(a) (b)

Fig. 2.20: Performance of the straw chambers: (a) detection efficiency; (b) position resolution.

The malfunction occurred right after the beginning of the data taking. The temperature at which the built-in electronics were operated was too high, even though it was within the manufacturer specifications.

(f) Hodoscopes

Three cylindrical plastic scintillator hodoscopes (H1, H2′ and H2) are located at increasing distances from the beam axis (Figure 2.15). They are employed in the trigger to select charged tracks. Their pulse heights, together with those in the Čerenkov counter, are used off-line to distinguish single charged particles from electron-positron pairs due to photon conversions or to Dalitz decays of neutral pions.

Hodoscope H1 is positioned right outside the beam pipe. It consists of 8 elements covering the polar angle between 9° and 65°. Each element is 2 mm thick. The 24 elements of hodoscope H2′ (scintillator thickness = 3 mm) are located at a radial distance of 6.5 cm. Hodoscope H2 is mounted on the frame of the Čerenkov counter and contains all the other inner detectors. The thickness of its 32 elements is 4 mm.

A fourth hodoscope, the forward veto counter FCH (Figure 2.11), is used in the trigger to reject events with charged tracks in the region not covered by the central detector. It comprises 8 trapezoidal plastic scintillators, which are perpendicular to the beam axis. They cover the full azimuth and the polar region 2°–9°.

All the hodoscope signals are sent to the trigger logic, to an ADC and to a TDC.

(g) Forward Calorimeter

The polar angle region from 2° to 12° is covered by a planar end-cap calorimeter (Hasan et al. 1990), shown in Figure 2.11 and in Figure 2.21. Its purpose is twofold: (a) to increase the acceptance for reactions like $\chi_0 \to J/\psi + \gamma \to (e^+e^-) + \gamma$ or $J/\psi + \pi^0 \to (e^+e^-) + (\gamma\gamma)$; (b) used as a veto, it can reduce the background to events completely contained in the central detector. It is not used in the form factor analysis presented here.

Its 144 modules are arranged according to a 13 × 13 array (10 cm spacing). There are no modules at the center of the grid (to accomodate the beam pipe) and at the corners, where angular coverage is already ensured by the central calorimeter. Each module consists of 148 alternate layers of lead plates and scintillator tiles, for a total of 14.7 radiation lengths of absorber.

During the shutdown of March 1997, the modules were replaced with lead-glass blocks, in order to obtain a better energy resolution. Since the

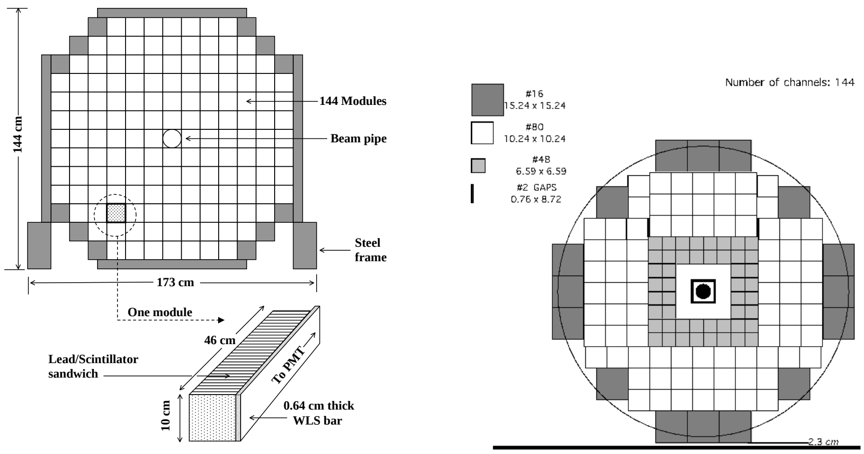

Fig. 2.21: The two end-cap calorimeters used in E-835: on the left, the layout of the scintillator/lead modules; on the right, the lead-glass calorimeter.

blocks have different sizes, the layout of the detector was modified (Bagnasco et al. 1997) (Figure 2.21).

The signal from each block is processed by a shaper board and then read out by an ADC and a TDC.

2.4 Data Acquisition

Including all the detector and trigger information (ADCs, TDCs, latches), each event occupies approximately 1 Kbyte, depending upon the data stream (charged or neutral events) and the CM energy. The total trigger rate is typically 1.4 KHz, yielding a rate to tape of the order of Mbytes/s.

E-835 employs the DART data acquisition system[i], which, in this regime, guarantees dead times smaller than 10%. The system performs several operations: event building, on-line filtering, data logging, run control and monitoring. The hardware is based upon the CAMAC/FASTBUS standards, while the software has been developed for SGI Challenge multiprocessor machines.

The data regarding the accelerator, the jet target and the luminosity monitor have their own individual collection streams, separated from the detector/trigger data.

[i] DART (`http://www-dart.fnal.gov`) is a collaboration between the Fermilab Computing Division and some fixed-target experiments.